Science Advances
AAAS

Supplementary Materials for

CLASP2 recognizes tubulins exposed at the microtubule plus-end in a nucleotide state–sensitive manner

Wangxi Luo *et al.*

Corresponding author: Ekaterina L. Grishchuk, gekate@pennmedicine.upenn.edu

Sci. Adv. **9**, eabq5404 (2023)
DOI: 10.1126/sciadv.abq5404

The PDF file includes:

Other Supplementary Material for this manuscript includes the following:

SUPPLEMENTARY NOTE

Putative GTP-binding site in the TOG2 domain of CLASP2 is not essential for microtubule interactions in vitro and in mitotic cells.

Work by Inoue et al. *(3)* identified sequences in *Drosophila* CLASP that match putative GTP-binding motifs: the NKLD sequence and Walker A-like sequence GGGTGTG (*46, 47*). Sequence alignment of CLASP2 proteins from different species revealed a high degree of conservation of NKxD sequence, with x represented by phenylalanine in human CLASP2 (Supplementary Fig. 6). However, there was no obvious Walker A sequence at the same location as in *Drosophila* CLASP or in other parts of CLASP2α. Because the amino acid composition of the GTP-binding pockets in different proteins is diverse, these alignments do not rule out that human CLASP2α can be regulated directly by GTP. Interestingly, the conserved NKxD motif localizes to the TOG2 domain, which is responsible for the microtubule-stabilizing activity of CLASP2 (*6*). To investigate whether the GTP-dependent microtubule-end binding by TOG2 in vitro requires the NKFD sequence, we replaced this site with the amino acid sequences NMFD and SKFS in the L-TOG2-S protein (see Materials and Methods). When conjugated to DNA scaffolds, these mutant proteins formed stable attachments to the ends of stabilized microtubule, but addition of soluble GTP caused rapid detachments (Supplementary Fig. 7 A,B). Thus, although the TOG2 domain appears to be the primary molecular determinant of GTP-sensitive microtubule end-on affinity, this interaction in vitro is not dependent on the NKFD sequence.

We then worked to discover any functional relevance of NKFD sequence for mitosis in human cells. We engineered a mutant CLASP2 sequence with SKFS and tested whether it can rescue RNAi knockdown of endogenous CLASP1 and 2 in U2OS cells (see Materials and Methods). In a recent study (*18*) it was shown that the smallest isoform of hCLASP2, CLASP2γ is sufficient to ensure all the normal functionalities of both CLASP1 and CLASP2 at the kinetochore-microtubule interface. In addition, it was also previously reported that disruption of soluble tubulin incorporation at the plus-ends of kinetochore microtubules in cells with CLASP depletion causes shortening of metaphase spindles (*14, 15, 44*), so we examined spindle phenotype in cells expressing the SKFS mutant. We found that the mean metaphase spindle length decreased very little in these cells: from 10.5 μm in the wild-type rescue to 10 μm (Supplementary Fig. 7 C,D). If GTPase activity were essential for a CLASP2 role at the kinetochore-microtubule interface, we would have expected a much stronger spindle shortening phenotype in the SKFS mutant, comparable with the disruption of the TOG2 domain (*18*). As a direct assessment of how the SKFS impacts the rate of tubulin incorporation at the kinetochore-embedded microtubule plus-ends, we measured the rate of poleward flux in these cells, but it was also unchanged (Supplementary Fig. 7E). Using fluorescence dissipation after photoactivation, we then examined microtubule turnover rate. This approach did not reveal any significant difference in the half-life of the kinetochore and non-kinetochore microtubules between parental cells and cells rescued with wild-type or SKFS mutant proteins (Supplementary Fig. 8). We concluded that the NFKD motif is dispensable for CLASP2´s role at the kinetochore-microtubule interface.

LEGENDS TO VIDEOS

Video 1. Microtubule binding to the clusters of CLASP2

TIRF imaging of the coverslip with immobilized DNA origami (blue), GFP-CLASP2α (green) seen as brighter dots colocalizing with DNA origami and dim dots representing randomly bound molecules, and rhodamine-labeled taxol-stabilized microtubules (red). Microtubules are seen as blurry vibrating spots; most of them remain near the clusters of CLASP2α for the entire imaging time (4.7 h). Scale bar 5 μm. See Data source file for more details about this and other videos.

Video 2. Microtubule binding to the clusters of Ndc80

Same experiment as in Video 1 but using GFP-tagged Ndc80 Broccoli. Microtubules rotate and slowly diffuse on the Ndc80 clusters during the 2-min imaging sequence. Scale bar 5 μm.

Video 3. Microtubule binding to the clusters of CLASP2α under flow

Same experiment as in Video 1 but a buffer is introduced into the chamber flowing from left to right. The removal of unbound microtubules clears the background, whereas the CLASP2α-tethered microtubules orient along the flow. The tethered microtubules start adopting their preferred orthogonal orientation when the flow is stopped later in this sequence, suggesting that the binding sites for CLASP2α are at the very termini of the microtubules. Scale bar 5 μm.

Video 4. Kinesin-dependent motion of microtubules away from the origami-**based clusters of CLASP2α**

Rhodamine-labeled taxol-stabilized microtubules were allowed to bind to GFP-CLASP2α (green) conjugated to origami nano-circles (blue), and the flow was introduced to promote microtubule reorientation and landing on the coverslip coated with Kinesin 1 motor. The video starts when ATP is introduced into the chamber; after a lag, microtubules begin to glide away from the CLASP2α clusters. Scale bar 5 μm.

Video 5. Unbinding of CLASP2α from the ends of microtubules that incorporate GTP-tubulin.

This video starts with rhodamine-labeled GMPCPP microtubule seeds (red) bound with their ends to the coverslip-immobilized clusters of GFP-CLASP2α (green). Hilyte647-labeled GTP-tubulin (grey) is then flowed into the chamber to trigger elongation of microtubules from the ends of the GMPCPP seeds. Majority of the microtubule seeds detach immediately and are removed by the flow, although one seed remains bound to origami, presumably due to a stochastic variation in the number and mode of the attached CLASP2α molecules. Subsequently, this seed alternates between two attachment modes to the CLASP2α cluster: the end-on and lateral binding modes. When microtubule seed is in the end-on orientation, the bound end shows no tubulin incorporation, suggesting that CLASP2α binding to the sites at the microtubule tip is not compatible with tubulin incorporation. However, when microtubule orients laterally presumably because some CLASP2α molecules are associated with the wall of this microtubule, its plus-end is freed to add and lose tubulin dimers. Scale bar 5 μm.

Video 6. Microtubule gliding with CLASP2α in solution.

This video is paused initially to show that Hilyte647 labeled taxol-stabilized microtubules (red) bind GFP-CLASP2α (1 nM, green) preferentially at one of the microtubule ends (white arrows). Additional weaker dots are seen along microtubule walls, at the opposite microtubule ends and also on the coverslip surface. Gliding is driven by the coverslip-associated Kinesin 1, and the brighter microtubule ends are trailing. Scale bar 5 μm.

Video 7. Dynamic microtubule coupled to CLASP2α-coated bead.

Video shows a short GMPCPP-stabilized microtubule seed labeled with Hilyte-647 (red) moving away from a coverslip-immobilized 1-μm bead coated with the GFP-labeled CLASP2α and the motor domains of CENP-E kinesin. To ensure visualization of the full range of motions, imaging was done via epi-fluorescence and in the presence of unlabeled soluble tubulin. Continuous motion of the seed away from the bead is associated with new tubulin incorporation at the bead-tethered microtubule plus-end, whereas angular deviations indicate temporary loss of the integrity of the bead-bound microtubule tip. Video plays 30 times faster than actual.

Video 8. Dynamic microtubule coupled to Ndc80-coated bead.

This video shows the same experiment as in Video 7 but using GFP-tagged Ndc80 Broccoli instead of CLASP2α *(37)*. Several red microtubule seeds are bound at the bead surface, with one of them moving repeatedly away and toward the bead with no significant pivoting. Video plays 30 times faster than actual. Scale bar 5 μm.

LEGENDS TO SUPPLEMENTARY FIGURES

Supplementary Fig. 1. Location of DNA origami handles and BG-oligos preparation.

A. DNA-origami designs rendered in caDNAno. The scaffold strand is in blue. Staples carrying 4 top handles, 8 inner handles, and 24 outer handles are shown in red, purple and orange, respectively. Handles (see Methods for sequences, not shown here for clarity) were extended from the 3' end of staple strands.

B. Negative-stain TEM image of the DNA-origami circles. Scale bar is 50 nm.

C. Schematic shows a cross-section of DNA origami ring with numbered DNA strands (yellow circles). Handles are distributed evenly along the ring's perimeter with total number of unique handles indicated.

D. Image of a polyacrylamide gel stained with SYBR Gold shows NH_2-oligos before and after reaction with BG-NHS. Successful labeling with BG is evident from the band shift to a higher molecular weight.

Supplementary Fig. 2. Single GFP molecule intensity measured through photobleaching analysis.

A. Representative photobleaching curves for non-specifically attached GFP-CLASP2α molecules.

B. Same as in panel A but for Ndc80-GFP Broccoli.

C. Distribution of intensities measured during photobleaching of GFP-CLASP2α molecules. Curves are equidistant Gaussian distributions. Distance between the peaks corresponds to average single molecule fluorescence intensity.

D. Same as in panel C but for Ndc80-GFP Broccoli.

E. Average single molecule fluorescence intensity acquired via the photobleaching analysis, as in panels A-D, and by collecting initial brightness of non-specific dots on the coverslip during experiments with origami scaffolds. Each point on the graph corresponds to average intensity determined in an independent experiment. Data for non-specific dots brightness is the same as in Figure 1G but with no normalization, see Data Source file for more details. Bars show mean ± SEM.

Supplementary Fig. 3. Origami-conjugated Ndc80 proteins support microtubule wall diffusion.

A. Representative tracks for microtubules diffusing on DNA origami-based clusters of Ndc80-GFP Broccoli.

B. Mean squared displacement for 20 microtubules with a liner fit (red line) and calculated diffusion coefficient.

Supplementary Fig. 4. Rupture force experiments to examine the strength of attachment between **CLASP2α** cluster and stabilized microtubule plus-end.

A. Lorentzian power spectrum for a 0.5 μm polystyrene bead in a static optical trap along (*z* axis) and perpendicular (*y* axis) to the laser beam.

B. Stiffness of the optical trap along *z* and *y* axes. Mean ± SD, n = 15 beads, each point corresponds to an individual bead.

C. Bead displacement at maximal force for experiments that ended with rupture (black symbols) and no rupture (gray symbols). The displacements along *z* axis are often significant, so they were taken into account when calculating total force acting on each bead.

D. Representative images illustrating experimental outcomes. Left images show polystyrene bead (grey) bound to microtubule (red) which has its end tethered to a cluster with CLASP2α (green). Images on the right show same fields but after force application with top images representing a lack of rupture, and bottom images showing a rupture between the cluster of CLASP2α and microtubule end. Bar is 1 μm.

E. Force application curves for two example experiments show contributions of *z* and *y* components. Data were acquired at 5 kHz and smoothed by averaging with sliding window of 50 points. Top and bottom graphs represent experiments with no rupture and with a rupture, correspondingly. Total force was calculated as a square root of sum of squares of the *z* and *y* force components.

Supplementary Fig. 5. Microtubule decoration by GFP-**CLASP2α in the presence of soluble** GTP.

Representative TIRF mages of taxol-stabilized microtubules (red) in the presence of 1.0 ± 0.2 nM full length human GFP-CLASP2α (green) and indicated concentration of Mg-GTP.

Supplementary Fig. 6. CLASP protein sequence and alignments.

A. Domain structure of *Drosophila* Orbit/Mast (uniport sequence Q9NBD7) and location of canonical sequences for GTP binding, as identified in *(3)*.

B. Alignment of protein sequences for CLASP2 orthologs from different species at the sites with NKxD motif. Sequences were aligned using ClustalO; numbers at the start of sequences correspond to amino acids in original protein sequences. Most proteins contain NKDF sequence, with dark green color showing identical amino acids and light green showing conservative replacements. In a logo-representation at the bottom of alignments, size of the letter corresponds to the frequency of amino acid encounter. Color shows amino acid charge (blue for negative, and red for positive).

C. Same as in panel B but showing protein alignment at the Walker A-like sequence. Protein sequence of *Drosophila* Orbit/Mast deviates significantly from sequences of other CLASP2 proteins and Walker A motif is lacking at this site.

D. PDB structure (3WOY) of *H. sapiens* TOG2 with NKFD motif shown in red.

E. Representative TIRF images of taxol-stabilized microtubules (red) incubated with 10 nM GFP-L-TOG2 or GFP-L-TOG2-*tubulin* proteins in buffer with no nucleotides. GFP-L-TOG2-*tubulin* protein, which contains two radical substitutions in tubulin-binding interface (W340E and K425A), shows no binding to microtubule walls and tips.

Supplementary Figure 7. Probing the role of putative GTP-binding site in TOG2 domain.

A. Still images from video recording of experiments in which L-TOG2-S SKFS mutant proteins were conjugated to the coverslip-immobilized DNA scaffolds and incubated with taxol-stabilized microtubules (left images), revealing strong end-binding preference. Images on the right were taken while flowing in the buffer with or without 1 mM GTP.

B. Kaplan–Meier survival plots for microtubule association with different protein clusters in the buffers with or without 1 mM GTP, see Data Source file for details.

C. Representative images of U2OS PA-GFP-α-tubulin cells. “CLASP1/2 RNAi” indicates cells treated with RNAi for both endogenous CLASP1 and CLASP2; mRPF-CLASP2γ was expressed with (SKFS) or without (WT) mutation of the NKFD motif, as indicated.

D. Quantification of mitotic spindle length: the first column represents the parental U2OS cell line and the remaining columns represent treatment with RNAi for both endogenous CLASP1 and CLASP2. Each data point represents an individual cell. Bars represent mean and standard deviation. Quantifications from 3 independent experiments: Parental Scramble RNAi= 133 cells; Parental CLASPs RNAi = 105 cells; SKFS mutant CLASPs RNAi = 155 cells; Wild Type CLASPs RNAi = 90 cells. ns = non-significant, * = $p<0.05$, ** = $p<0.01$, **** = $p<0.0001$, t-test.

E. Quantification of spindle poleward flux. The first column corresponds to the parental cell line, and the remaining columns correspond to mRPF-CLASP2γ expressing cell lines after endogenous CLASP1 and CLASP2 depletion. Boxes represent median and interquartile interval; bars represent minimum and maximum values. Parental = 10 cells, pool of 3 independent experiments; SKFS mutant = 24 cells, pool of 5 independent experiments; Wild Type = 8 cells, pool of 3 independent experiments. ns = non-significant, Mann-Whitney U-Test.

Supplementary Fig. 8. Lack of the strong effects from the SKFS mutation of CLASP2 in dividing cells.

A. Photoactivation experiments in live U2OS parental PA-GFP-α-tubulin cells expressing the mRFP-CLASP2γ constructs after CLASPs RNAi; Panels represent DIC, the mRFP-CLASP2γ signal (red) and the PA-GFP-α-tubulin signal before photoactivation (Pre-PA), immediately after photoactivation (PA) and at 2 and 4.5 min after photoactivation. The PA-GFP-α-tubulin signal was inverted for better visualization. Scale bar is 5 μm.

B, C. Quantification of half-life of spindle microtubules in the studied cell lines: kinetochores microtubules (KT-MT, panel B) and non-kinetochore microtubules (non KT-MT, panel C). See legend to Supplementary Fig. 7 C-E for more details.

Supplementary Fig. 9. Nucleotide **and CLASP2α** binding to stabilized microtubule ends.

A. GFP intensity of microtubule ends decorated with GFP-CLASP2α. Taxol-stabilized microtubules were incubated with GFP-CLASP2α (1 nM) and indicated GTP nucleotide (100 nM). Each dot represents median brightness from an independent experiment, see Data Source file for details. Error bars are SEMs, ** p<0.01, *** p<0.001, ns - no significant difference, t-test.

B. Representative images of a taxol-stabilized microtubule (labeled with Hilyte647) incubated with 1 nM GFP-CLASP2α and 100 nM Cy3-GTP. Yellow squares indicate regions for intensity analyses.

C. Intensity of microtubule ends incubated with a mixture of GFP-CLASP2α and Cy3-GTP, as illustrated in panel B. Each dot represents average brightness with SE of microtubule ends observed in chambers incubated with different mixtures of GFP-CLASP2α (varied from 1.10 to 1.75 nM) and Cy3-GTP (varied from 88 to 119 nM). Linear fitting (blue line) suggests anti-correlation between GTP and CLASP2α microtubule tip-association.

D. Intensity of stabilized microtubule ends incubated with 100 nM Cy3-GTP alone (no competition), or in combination with 1 μM GTP or GDP (both unlabeled). Each dot represents median brightness from an independent experiment, see Data Source file for details. Error bars are SEMs, ** p<0.01, t-test.

Supplementary Fig. 10. Microtubule decoration by GFP-tagged proteins.

Representative TIRF images show taxol-stabilized microtubules (red) incubated in the presence of indicated concentrations of GFP-tagged full length human CLASP2α (top set of images) or human Ndc80 Broccoli (lower set of images).

Supplementary Fig. 11. Characterization of the dynamics of microtubule plus-ends tethered by beads with different molecular composition.

A. Schematic of the experimental assay in which initial lateral attachment of the GMPCPP-stabilized microtubule seeds is converted into the end-on attachments via the combined activity of the bead-conjugated CENP-E kinesin and a microtubule wall-diffusing protein. Black arrow shows the direction of the walking motor, which drives microtubule gliding until the motor reaches the microtubule plus-end. In the presence of soluble GTP-tubulin, subsequent microtubule motion takes place simultaneously with tubulin dynamics at the bead-tethered end. Dynamics of this end and its mechanical rigidity are deduced from the directional and sideways motions of the labeled seed (in red).

B. Frequency of the observed dynamic states for the microtubule ends coupled to beads coated with CENP-E and indicated MAP; data are based on N=4 for Ndc80, N=4 for CLASP2, N=3 for EB1. Fraction of dynamic attachments was calculated from the total number n (given for each column) of bead-bound microtubules. Fraction of microtubules that switched into depolymerization is from the total number n of polymerizing microtubules. Fraction of regrowth events is from the total number n of depolymerizing microtubules. n/a – not applicable or no such events were observed.

C. Dynamic parameters for the freely growing microtubule plus-ends (N=4) and for the plus ends coupled to the protein-coated beads, as in panel B. Quantifications for the depolymerization rate (left panel), microtubule polymerization phase (middle two graphs) and total duration of the dynamic microtubule end attachment (last graph).

Columns (Mean ± SEM) are calculated based on N≥3 independent experiments and n examined microtubules (noted at each column) *p<0.05 (Mann-Whitney u test); n/a – not applicable or no such events were observed.

Supplementary Fig. 12. Mechanics of the bead-coupled dynamic microtubule plus-end.

A. Examples of trajectories and corresponding length vs. time plots for the distal end of Hylite647-labeled microtubule segment (seed), see main text for more details. First panels for Ndc80 and CLASP2α are same as in Fig. 7 C and D, but depicting more details about microtubule end dynamics. Black parts of the trajectories correspond to the polymerization-coupled movement of microtubule end, and red color for depolymerization. Ndc80 and EB1 proteins support coupling of both elongating and shortening microtubules, whereas no depolymerization was observed with CLASP2-containing beads.

B. Example histogram of the pivoting angles for one microtubule coupled with CENP-E and EB1. Half-width of the Gaussian fitting, represented with parameter σ, was used as a measure (in degrees) of the directional instability of the coupled microtubule plus-ends.

Supplementary Fig. 13. Proposed mechanism of CLASP2-dependent elongation of kinetochore microtubules.

A. Structural model of human CLASP1 TOG2 domain complex with αβ-tubulin dimer (reproduced with modifications from *(27)*) showing approximate locations of GTP-bindings sites in tubulin monomers and the NKFD motif in TOG2 domain.

B. Plus-ends of kinetochore microtubules are coupled to kinetochore with the help of numerous proteins, but this simplified schematics depicts only kinetochore-associated Ndc80 complex and CLASP2, as well as soluble EB proteins. CLASP2 is enriched at kinetochore-bound microtubule ends owing to its localization at the kinetochore and via the EB-dependent recruitment. Microtubule wall diffusion of CLASP2 may also increase its chances to encounter the “rogue” tubulins at the microtubule tip. When terminal GDP-tubulin becomes exposed, the TOG2 domain of CLASP2 forms a strong bond and stabilizes this dimer temporarily until its associated GDP is replaced with GTP. TOG2 is then released and the protofilament with now terminal GTP-tubulin resumes its normal assembly, while continuously tethered to kinetochore by proteins like Ndc80.

C. Schematic of three terminal tubulins (open circles) at the plus-end of a microtubule cylinder viewed from that end before (open circles) and after (colored circles) outward bending of the central subunit. Left: yellow circle shows position of the central β-tubulin monomer after it tilted away from the microtubule lumen at angle φ from the radial axis. The displacement shown corresponds to the intra-dimer bending angle of 18^{o}, which matches the curvature of TOG2 domain (blue) and has a larger interaction surface than in panel A. Right: twisting motion of the terminal GDP dimer may permit a direct lateral contact (red) between the dimer-associated TOG2 domain and another tubulin dimer in adjacent protofilament. Angles and displacements for this schematics were estimated based on *(27, 66)*.

A

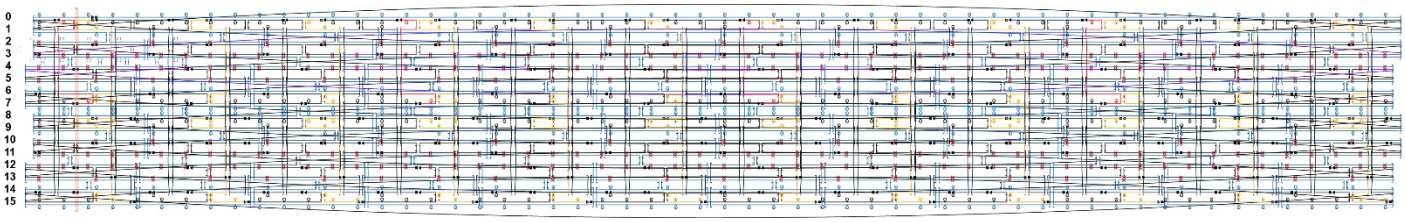

B

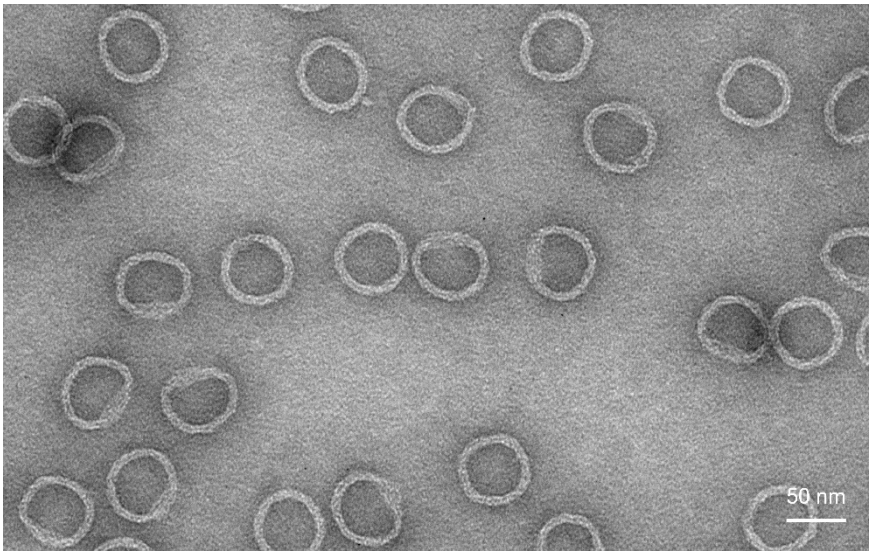

C

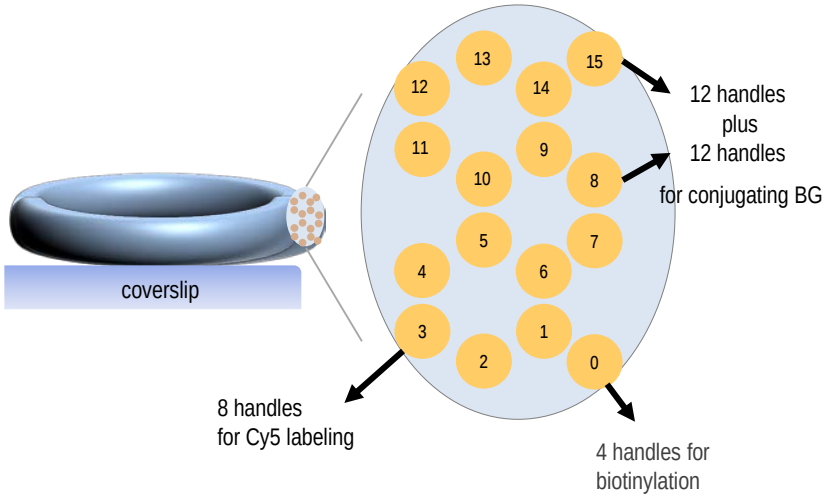

D

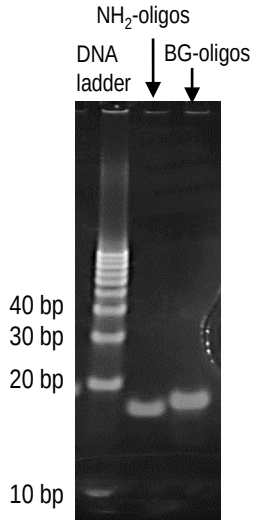

Supplementary Figure 1

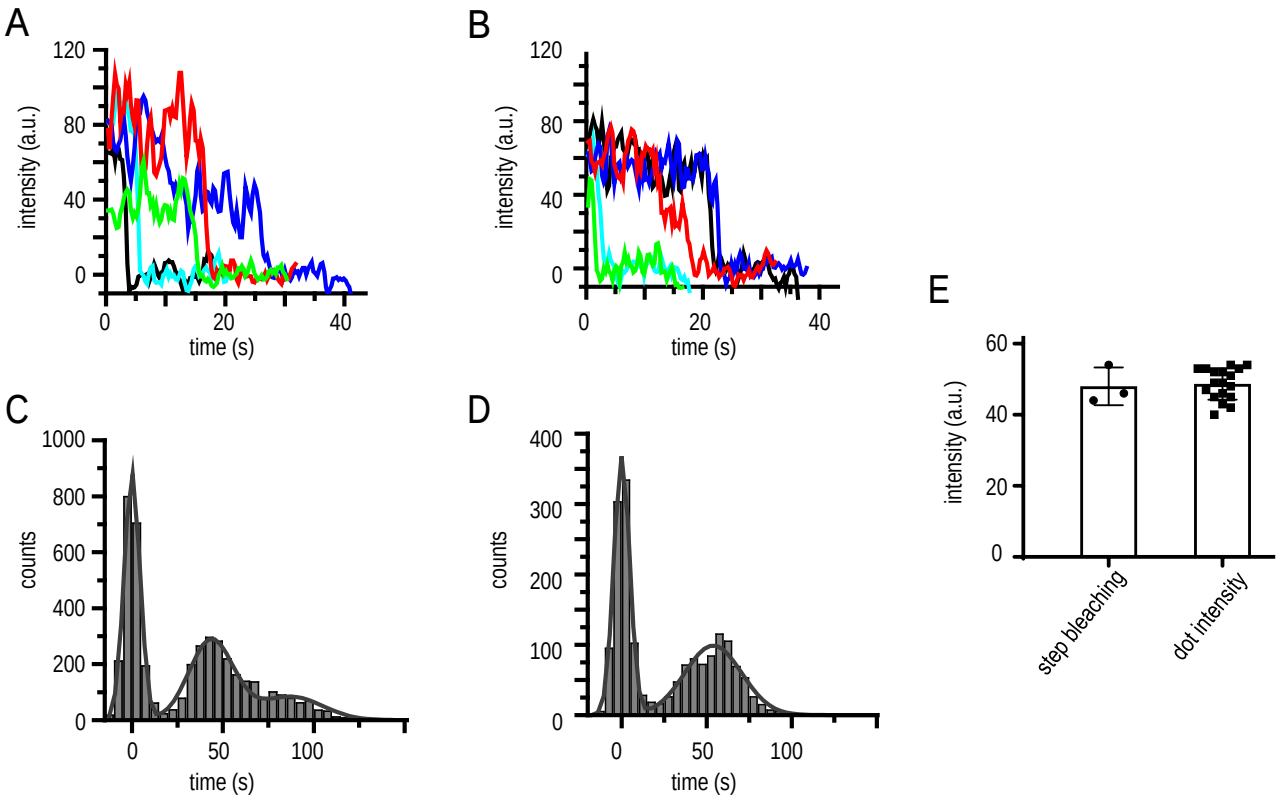

Supplementary Figure 2

A

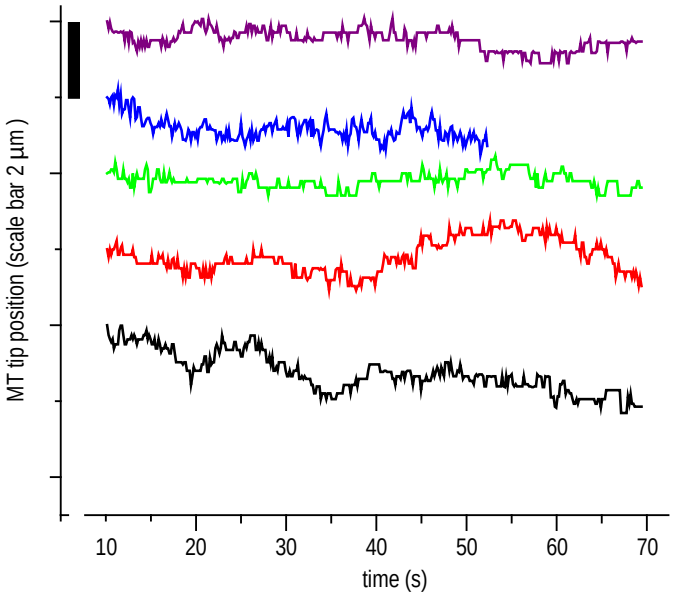

B

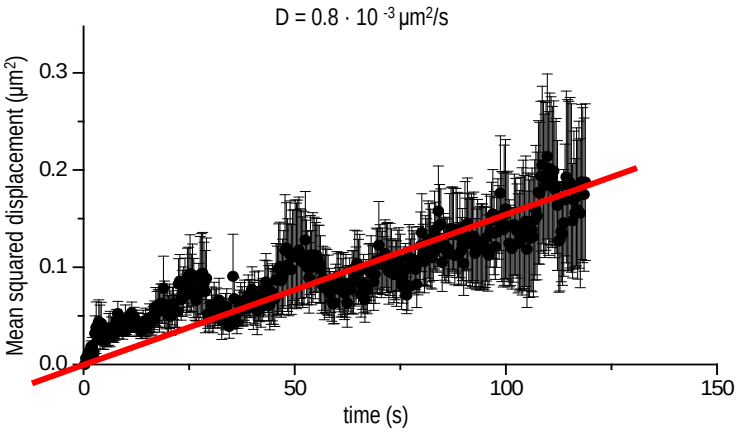

Supplementary Figure 3

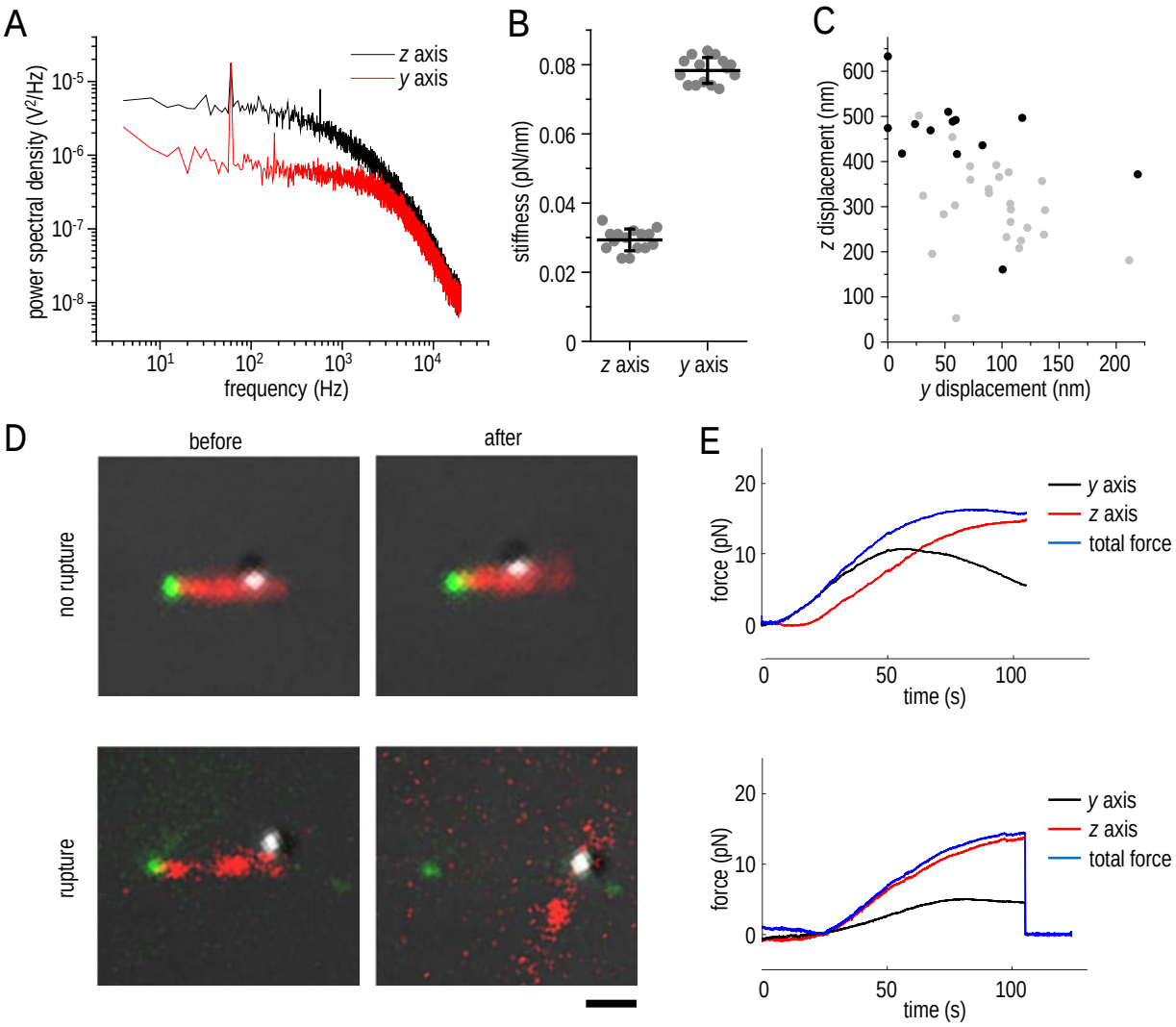

Supplementary Figure 4

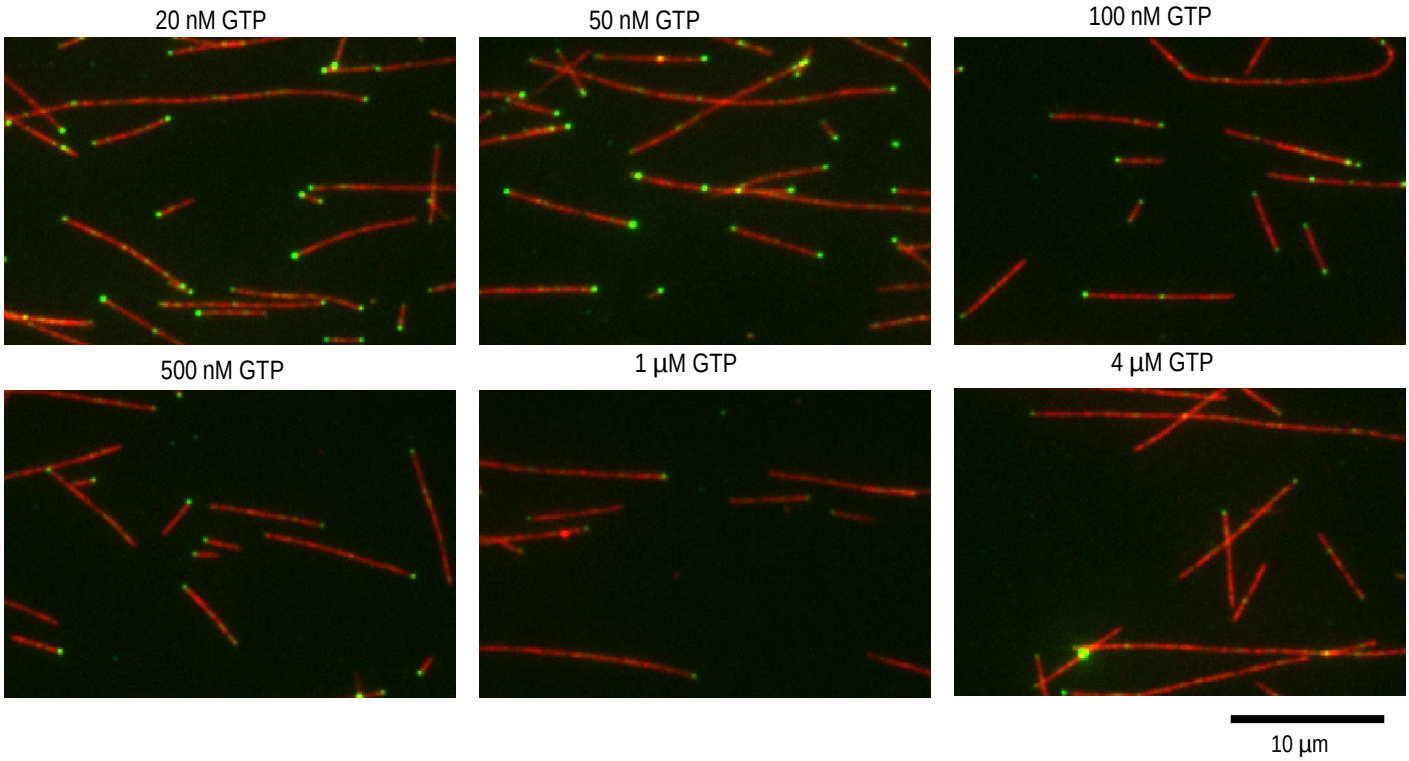

Supplementary Figure 5

A

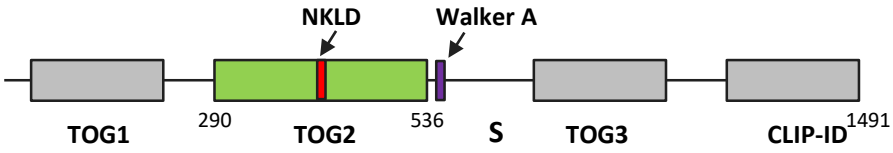

B

				DB reference
D.melanogaster	Orbit/mast	397	LRNKLDAFCW	NCBI NP_524651.2
H.sapiens	CLASP2α	401	LGNKFDHGAE	UniProtKB O75122-3
H.sapiens	CLASP2β	173	LGNKFDHGAE	UniProtKB O75122-2
H.sapiens	CLASP2γ	167	LGNKFDHGAE	UniProtKB O75122
G.gallus	CLASP2	401	LGNKFDHGAE	NCBI XP_025002997.2
D.rerio	CLASP2	400	LGNKFDHGAE	NCBI XP_021323713.1
M.musculus	CLASP2	173	LGNKFDHGAE	NCBI AAI41416.1
C.elegans	CLASP2	122	FGTDVRQIAE	NCBI CCO25650.1

C

```
D.m. 527 LDIAAQRALEREREGGGGGGTGTGTGTA----------P---------------ETRRTVSRIGRTPGTLQ
H.s. 530 LEPSYQKSLQTYLKSSGSVASLPQSDRSSSSSQESLNRPFSSKWSTANPSTVAGRVSAGSSKASSLPGSLQ
H.s. 302 LEPSYQKSLQTYLKSSGSVASLPQSDRSSSSSQESLNRPFSSKWSTANPSTVAGRVSAGSSKASSLPGSLQ
H.s. 296 LEPSYQKSLQTYLKSSGSVASLPQSDRSSSSSQESLNRPFSSKWSTANPSTVAGRVSAGSSKASSLPGSLQ
G.g. 528 LEPPYQRSLQTYLKNSGSIASLPQSDRSSSSSQESLNRPLSSKWSAASPASFAGRVS-GSSKSVPSPGTLQ
D.r. 529 LESSYQRTLQSCLKSSGSVASLPQSDRSSSSSQESLNRPLS-KWSAAPG-----RVP-AGSKSSGSPASLQ
M.m. 302 LEPSYQKSLQTYLKSSGSVASLPQSDRSSSSSQESLNRPFSSKWSTANPSTVAGRVSVGGSKANPLPGSLQ
C.e. 249 VDSSKQKMLRASDAASSSTSINSERG----------TAPFRSKLSAGSIGGIRN----------APN-IS
```

D

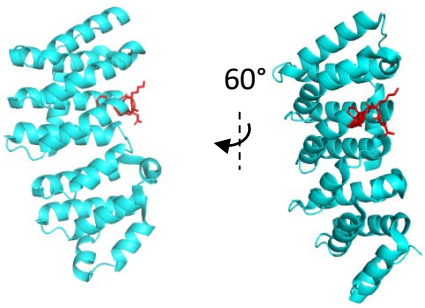

E

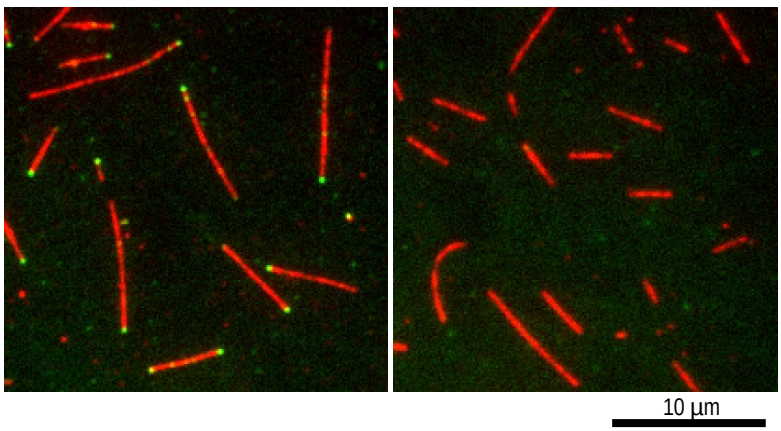

Supplementary Figure 6

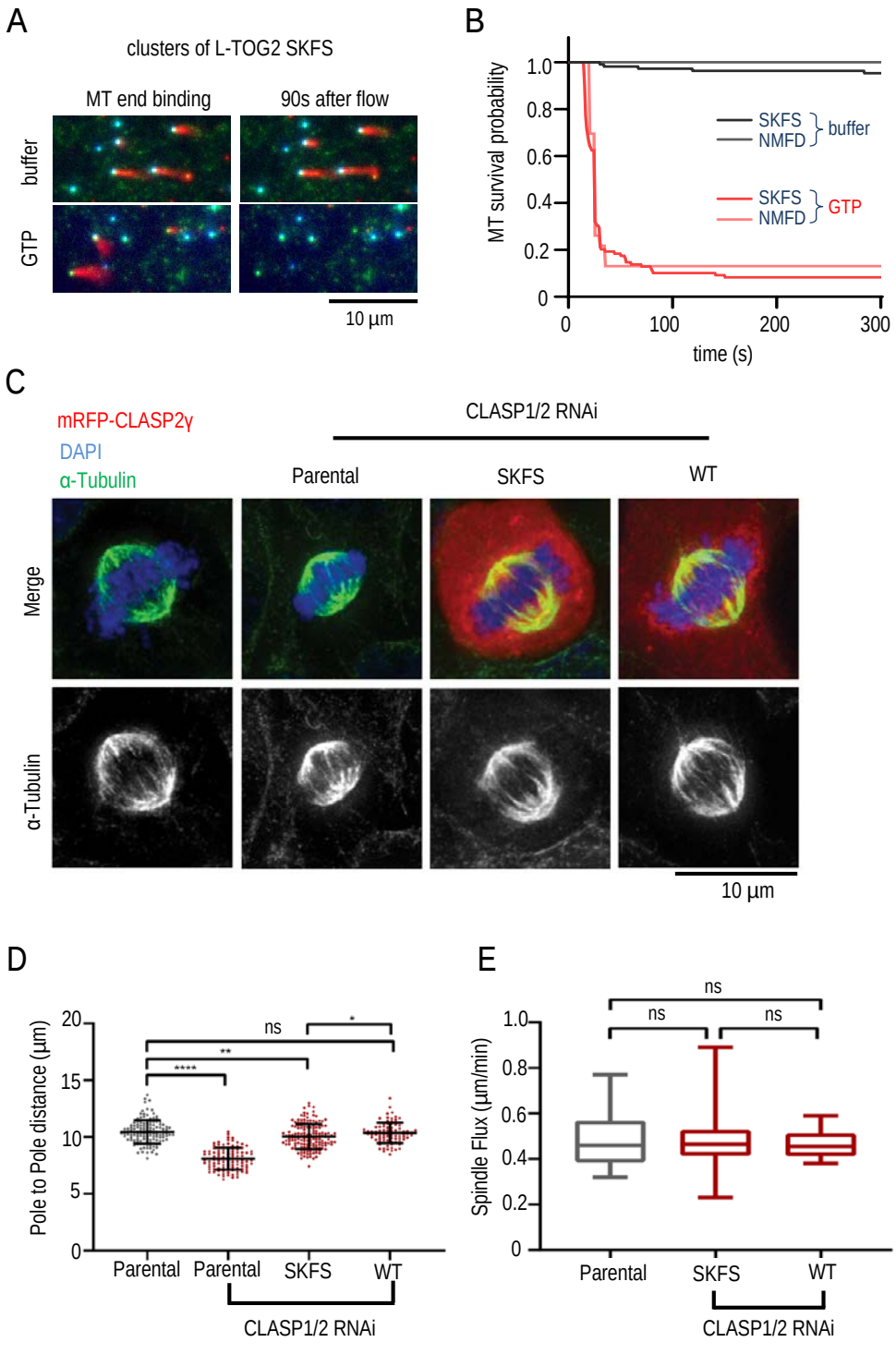

Supplementary Figure 7

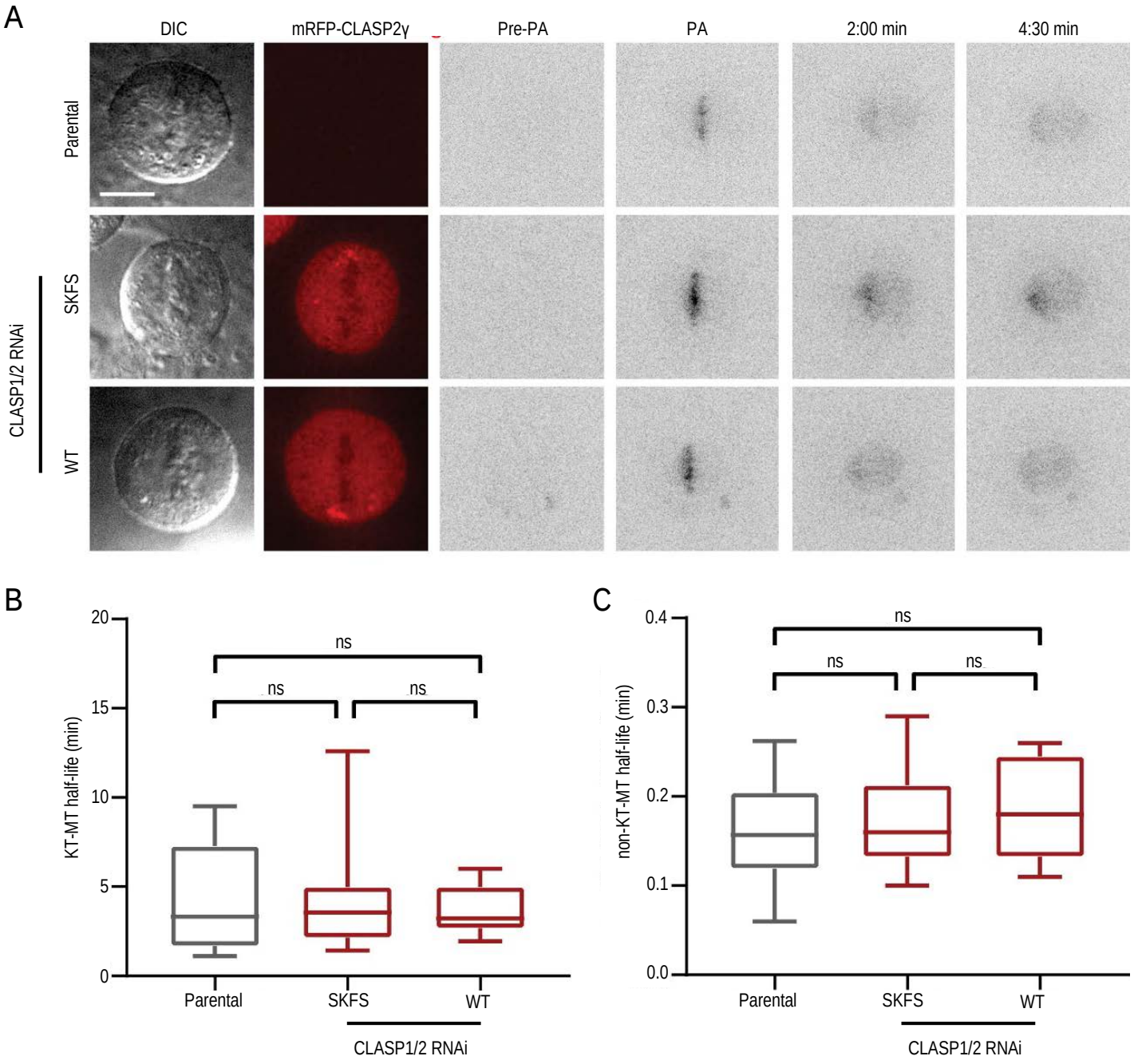

Supplementary Figure 8

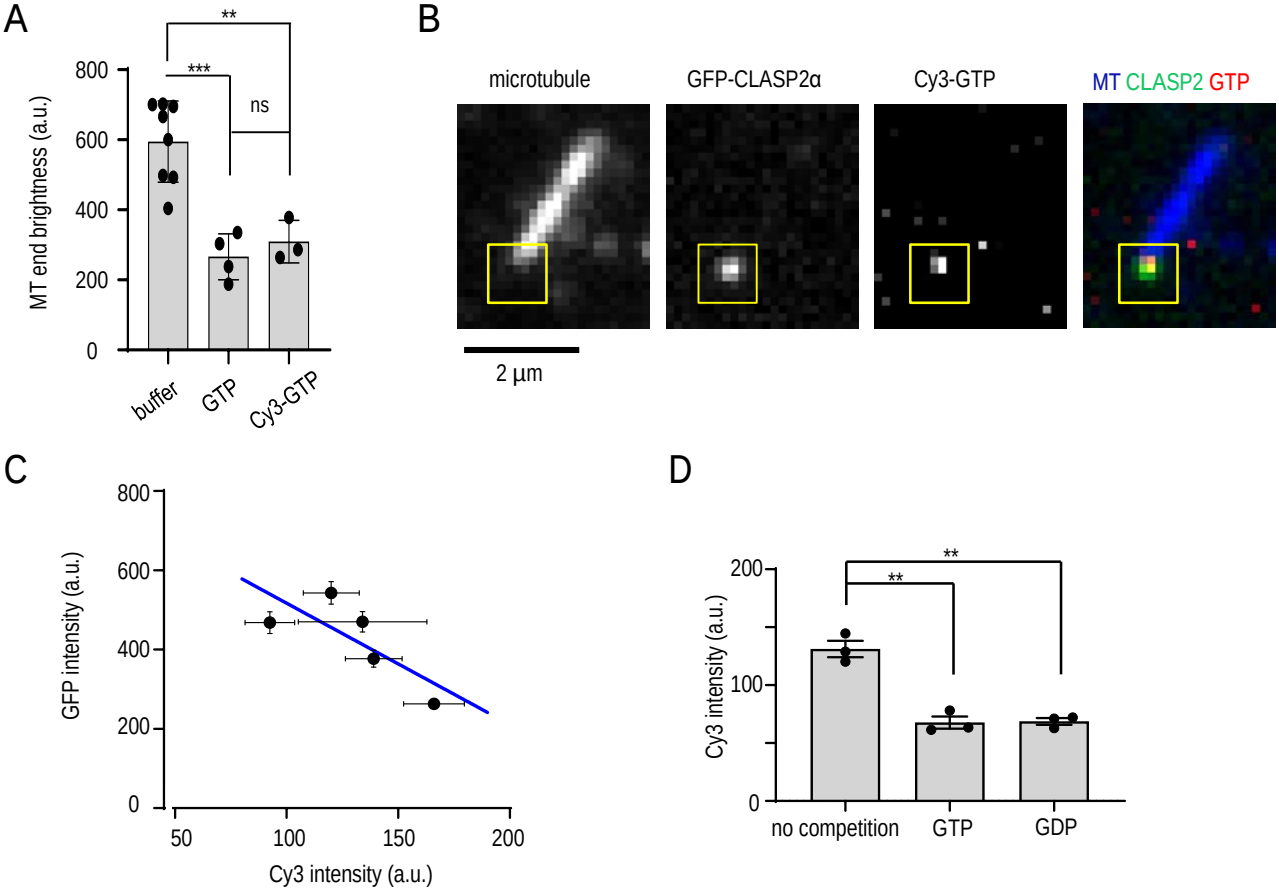

Supplementary Figure 9

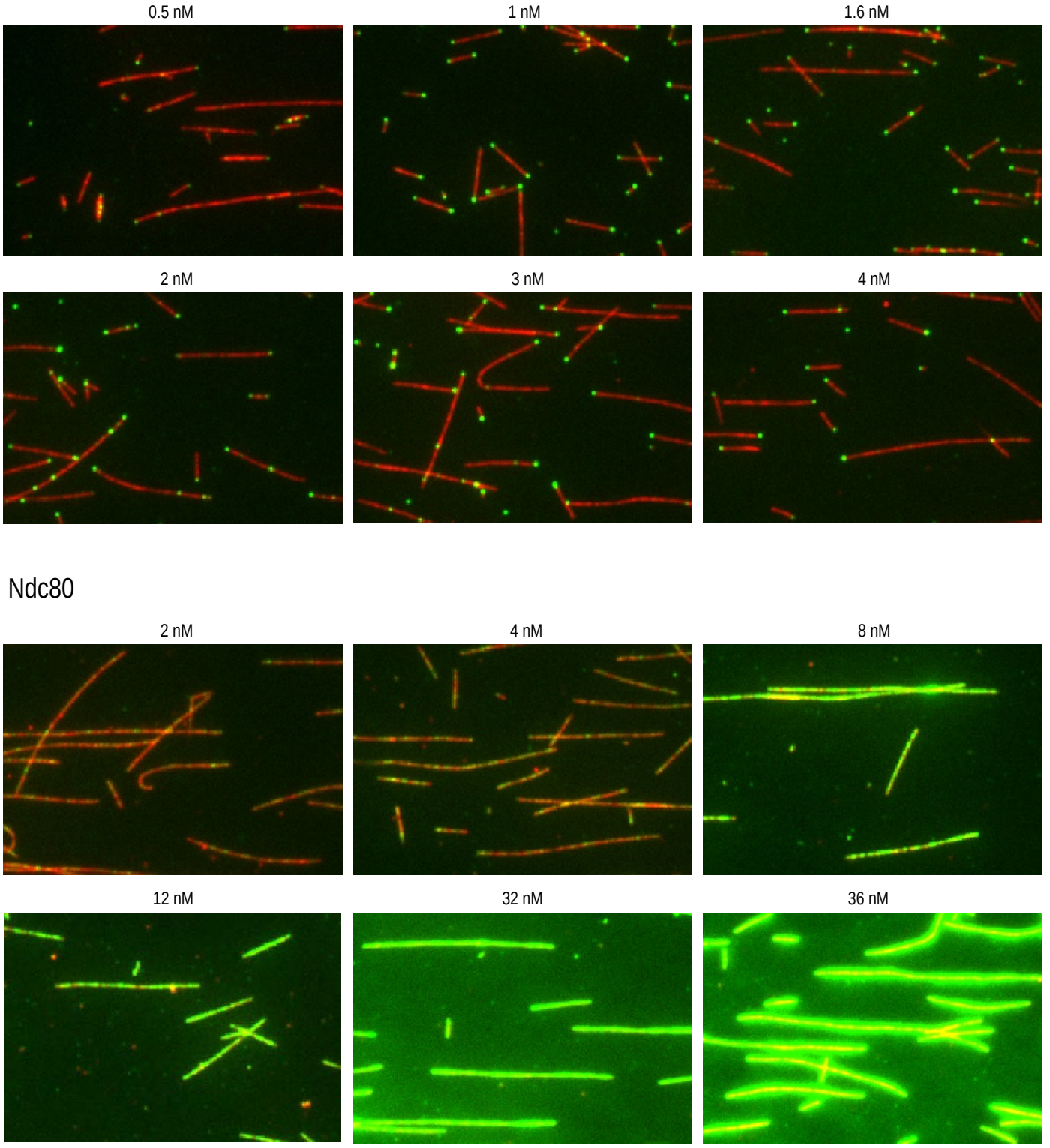

Supplementary Figure 10

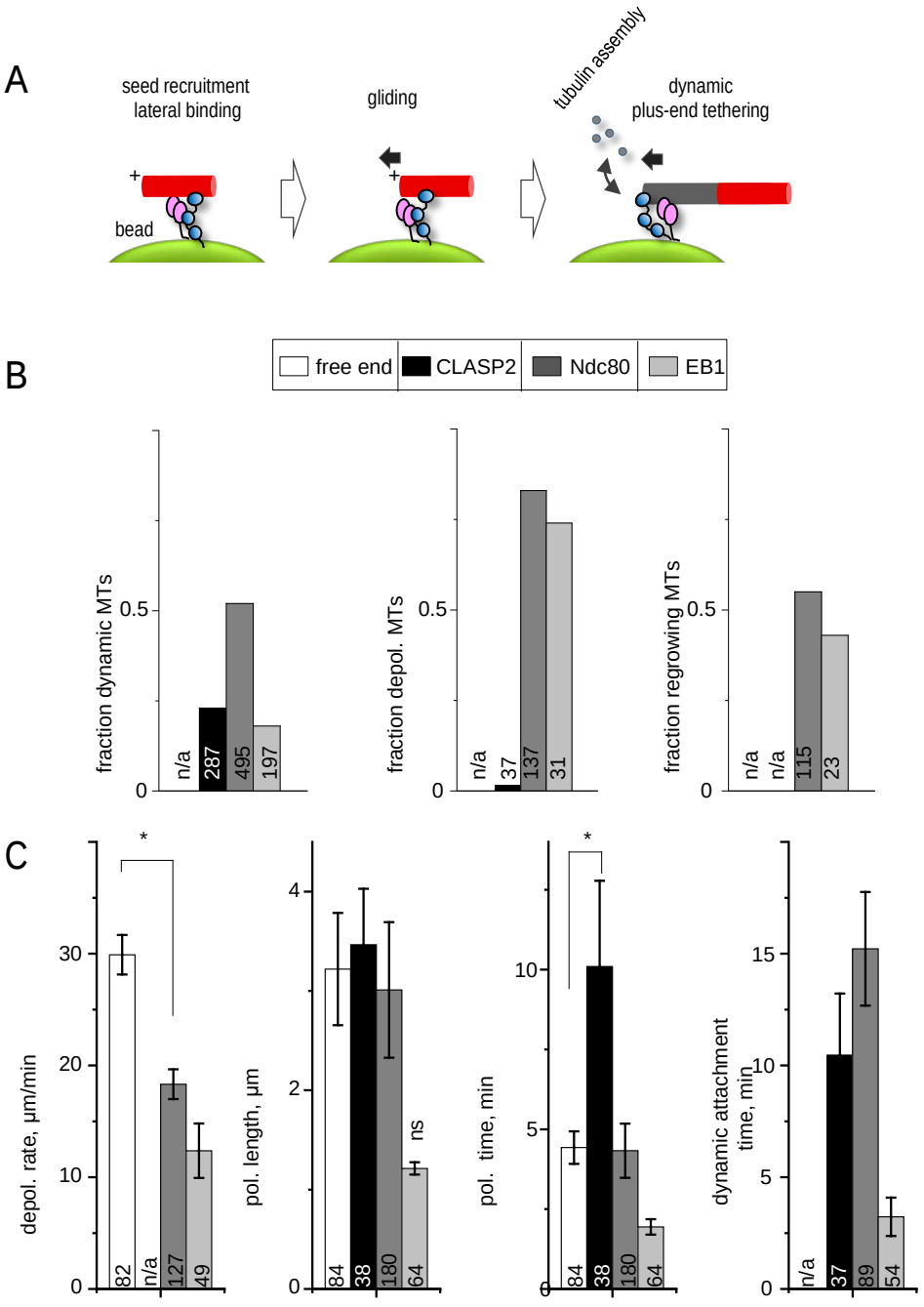

Supplementary Figure 11

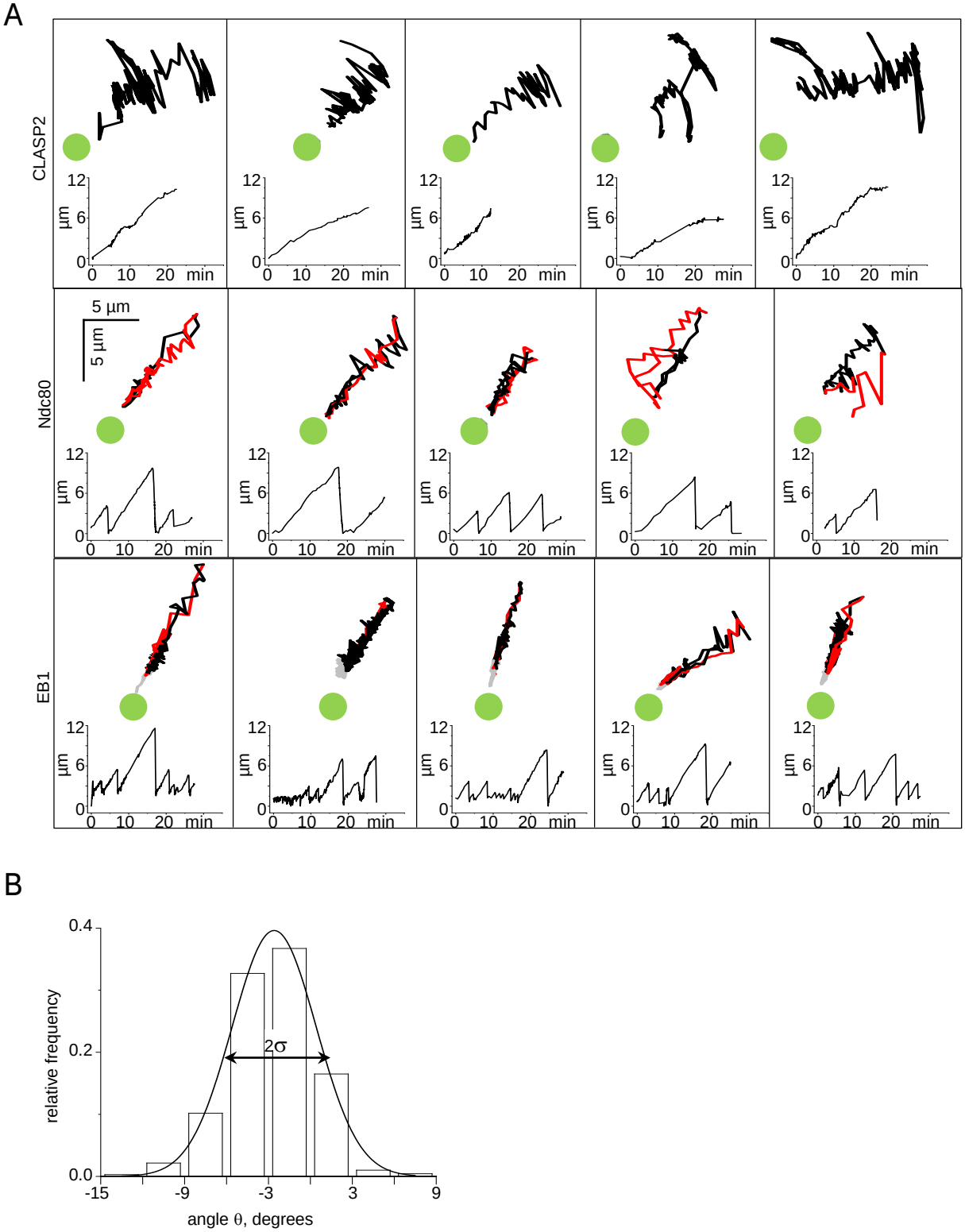

Supplementary Figure 12

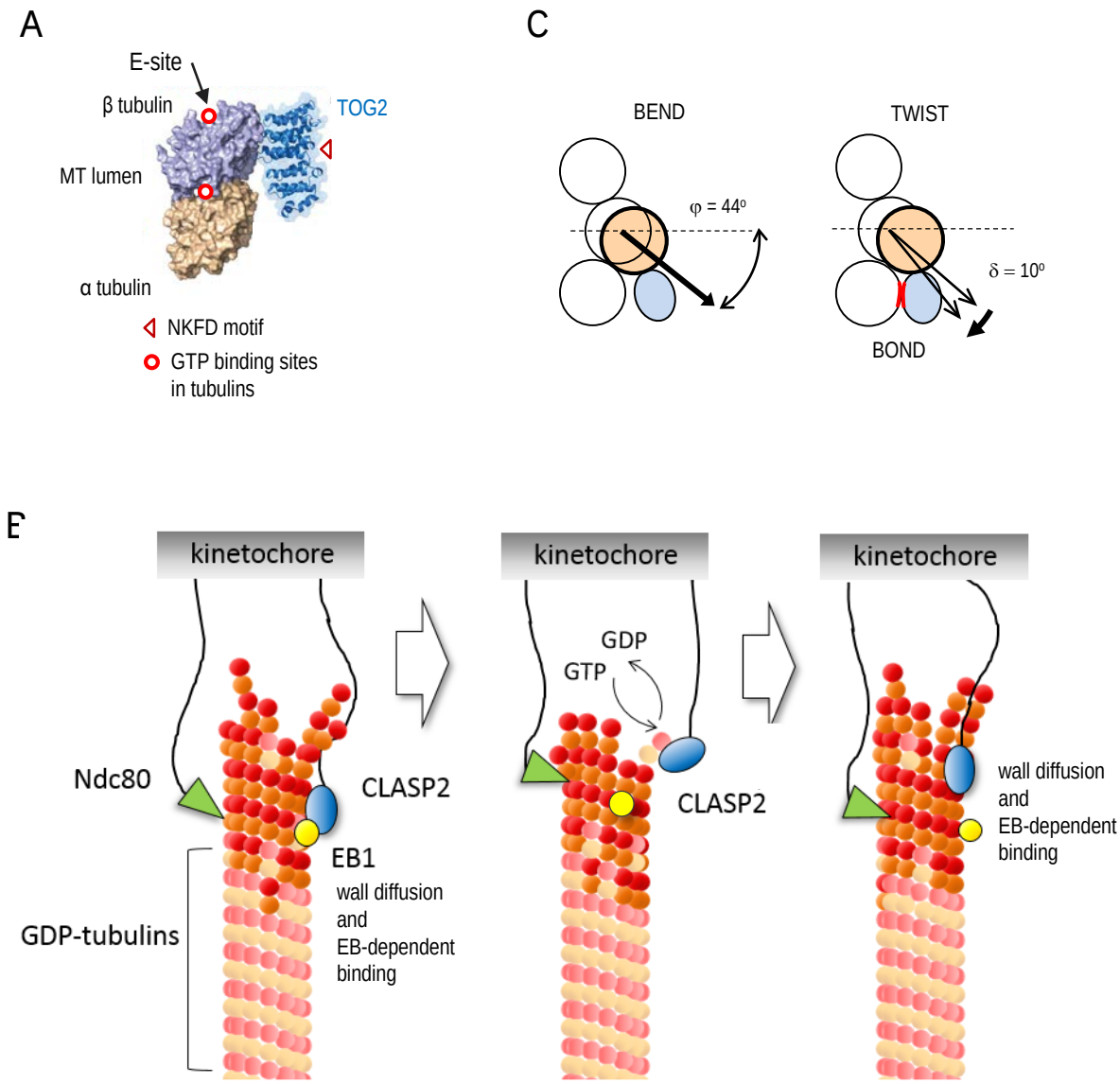

Supplementary Figure 13